

# Deposition-evaporation dynamics of hard rods in 2-d: Orientational correlations and the effect of spatial gradients

Mahendra D. Khandkar and Mustansir Barma

*Department of Theoretical Physics, Tata Institute of Fundamental Research,  
Homi Bhabha Road, Colaba, Mumbai-400 005, INDIA.*

(Dated: February 8, 2020)

Deposition and evaporation of infinitely thin hard rods (needles) is studied in two dimensions using Monte Carlo simulations. The ratio of deposition to evaporation rates controls the equilibrium density of rods, and increasing it leads to an entropy-driven transition to a nematic phase in which both static and dynamical orientational correlation functions decay as power laws, with exponents varying continuously with deposition-evaporation rate ratio. Our results for the onset of the power-law phase agree with those for a conserved number of rods. At a coarse-grained level, the dynamics of the non-conserved angle field is described by the Edwards-Wilkinson equation. Predicted relations between the exponents of the quadrupolar and octupolar correlation functions are borne out by our numerical results. We explore the effects of spatial inhomogeneity in the deposition-evaporation ratio by simulations, entropy-based arguments and a study of the new terms introduced in the free energy. The primary effect is that needles tend to align along the local spatial gradient of the ratio. A uniform gradient thus induces a uniformly aligned state, as does a gradient which varies randomly in magnitude and sign, but acts only in one direction. Random variations of deposition-evaporation rates in both directions induce frustration, resulting in a state with glassy characteristics.

## I. INTRODUCTION

An assembly of particles interacting via hard-core repulsion serves as a useful model for studying simple fluids, colloids, liquid crystals and many other soft matter systems. The analysis of such model systems helps in understanding the features of real systems, such as their phase behaviour, structural and dynamic properties. An important role is played by the anisotropy of shape of the constituent particles, which can range from thick elongated platelets to thin rods. Some examples of systems in which the constituent particles show anisotropy are certain types of colloids, liquid crystals and protein molecules. In particular, rod-like particles are found in suspensions of the tobacco mosaic virus [1], nematic liquid crystals [2] and, recently, carbon nanotube gels [3]. All these systems show very rich and characteristic phase behaviour.

Rod-like particles have been modeled theoretically as ellipses [4], rectangles and spherocylinders [5, 6, 7] with varying aspect ratios, a limiting case being infinitely thin hard rods or needles [8]. These systems exhibit a number of interesting entropy-driven phase transitions which have been studied in two and three dimensions, usually using simulations with number-conserving dynamics. On the other hand, there are a number of physical processes which involve adsorption (deposition) and desorption (evaporation) of particles, which do not conserve particle number and which are important for some monolayer growth processes. Adsorption and desorption are also important in the binding/unbinding of ligands to microtubules, the interaction of proteins with DNA [9, 10] and many catalytic reactions. Finally, in recent experiments on assemblies of long objects (rice grains, thin copper rods tapered at the ends) on a vibrating plate [11], individual particles jump off and return to the plate, lead-

ing ultimately to a state with interesting patterns. These considerations motivate us to study the deposition and evaporation of hard objects with rigid boundaries on a substrate. While a deposition-only system, of the type studied in random sequential adsorption [9], can end up in a non-evolving jammed configuration, with the addition of evaporation, the system eventually reaches a very different equilibrium state with a density governed by the rates of deposition and evaporation [12-17]. Specifically, we study the deposition and evaporation of infinitely thin needles on a 2D substrate. The hard core constraint is enforced by rejecting any deposition event which results in an overlap of needles.

It is useful to recall some known facts about a system of hard needles with no externally imposed spatial inhomogeneities. This system shows a transition from a low-density orientationally disordered (isotropic) state to a high-density ordered state with nematic correlations. This transition, whose existence was pointed out by Onsager [18], can be viewed as an outcome of the interplay between orientational and translational entropy of the needles; the ordered (aligned) state is preferred at high density since alignment leads to an increase of translational entropy, albeit at the cost of orientational entropy. The nature of the orientational ordering is dimension-dependent. In three dimensions, orientational long range order (LRO) sets in. A state with LRO would break the continuous symmetry of rotations, and is thus not expected to occur in 2D, even though the Mermin-Wagner theorem cannot be generalized to this system [19]. Indeed, the simulation study of Frenkel and Eppenga [8] on a system with a fixed number of needles confirms the absence of LRO in 2D, and finds a phase with power-law decays of orientational correlations, quite analogously to the XY model [20].

On a coarse-grained scale, the local orientation at loca-

tion  $\mathbf{r}$  and time  $t$  is specified by an angle field  $\theta(\mathbf{r}, t)$ . The orientational correlation functions of interest are defined as

$$g_\ell(\mathbf{r}, t) = \langle \cos[\ell(\theta(\mathbf{r}, t) - \theta(0, 0))] \rangle \quad (1)$$

where  $\ell$  is an even integer, and  $\theta$  and  $\theta + \pi$  represent the same state. Quadrupolar correlations are probed by  $\ell = 2$ , whereas higher values of  $\ell$  correspond to higher multipolarities. From numerical simulations, we find power law decays in both space and time:  $g_\ell(r, 0) \sim r^{-\eta_\ell}$  and  $g_\ell(0, t) \sim t^{-\beta_\ell}$  for both  $\ell = 2$  and 4. Our results for the static correlations conform to the Kosterlitz-Thouless theory for the onset of correlations, while our results for the dynamics show that their decay in time is governed by the Edwards-Wilkinson equation.

We also study spatial variations of the deposition rate, and find strong effects on the nature of the ordering. We consider several types of variations: (i) a sharp change across a linear interface; (ii) a smooth linear gradient; (iii) a random variation of rates in one direction and (iv) random variation of rates in the plane. We find that the qualitative effect of spatial variations is to induce alignment of needles in the direction of gradient, an effect with an entropic origin. In (i), the effect dies down slowly with increasing distance from the interface, but in cases (ii) and (iii) it results in a state with overall alignment along the direction of variation of the deposition rate. The random variation in (iv) induces frustration and the result is then a state with glassy features such as strong initial condition dependence and slow relaxation.

## II. MODEL AND PROCEDURE

In our model, infinitely thin hard rods (needles) are added to a 2D substrate with area  $A$  under the effect of a constant attempt rate, and simultaneously removed randomly from the substrate with a specified rate. In a deposition attempt, the location of the centre of mass of the needle is chosen at random on the substrate, and the orientation angle is chosen at random as well. Let  $\Gamma_d$  be the rate of deposition attempts per unit area per unit angle interval. An attempt is successful only if the depositing needle in question would not overlap with existing needles on the substrate.

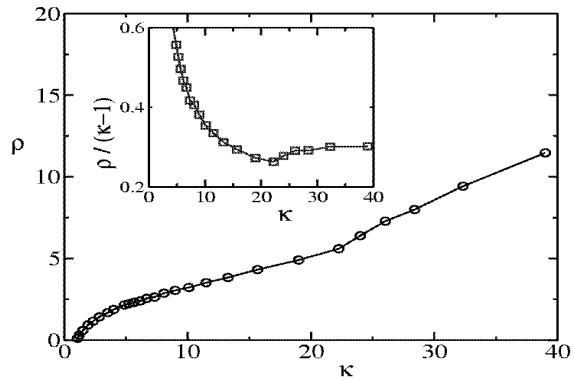
While considering evaporation, we may consider either a needle-based or position-based process. In the former, a needle is chosen at random from those present on the substrate and then removed. If the total rate of such removals is  $R_e$  we may associate a removal rate  $\gamma_e = \frac{R_e}{2\pi A}$  per unit area per unit angle interval. To define a position-based evaporation process, we divide the substrate into elements of an area  $a$  which are small enough that there is a negligible probability that the centre of mass of more than one needle is present in each. Let  $\Gamma_e^a$  be the evaporation attempt rate per element per angle interval. The corresponding attempt rate per unit area is  $\Gamma_e^a/a$ .

Under deposition-evaporation dynamics, the system eventually reaches a steady state with an average density  $\rho$  rods per unit area. The value of  $\rho$  depends on the ratio of  $\Gamma_d$  to either  $\gamma_e$  or  $\Gamma_e^a$ , depending on which evaporation procedure has been adopted. In the steady state, since only a fraction  $\rho a$  of elements is occupied by needle centres of masses, the rate of successful evaporation is  $\Gamma_e^a \rho$  which is thus equal to  $\gamma_e$ .

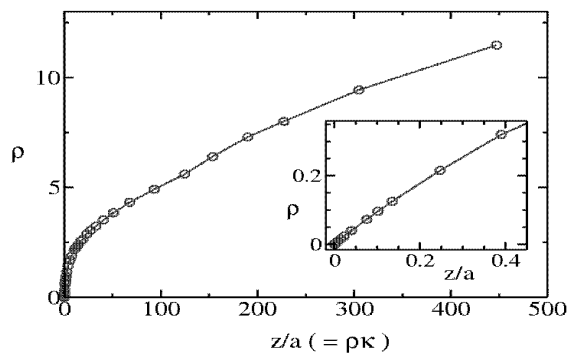
If we associate a fugacity  $z$  with each needle, the weight of an  $N$ -needle configuration  $C$  in steady state is  $z^N$ . If  $C'$  is an  $(N-1)$ -needle configuration obtained by removing a particular needle from a specified element within an angular interval  $\delta\theta$  from  $C$ , then it is easy to see that the condition of detailed balance between  $C$  and  $C'$  is met provided that  $\Gamma_e^a z^N = a\Gamma_d z^{N-1}$ , i.e.  $z = a\Gamma_d/\Gamma_e = \rho a \Gamma_d/\gamma_e$ . This holds for every pair of connected configurations  $(C, C')$  implying that the steady state is a grand canonical equilibrium state.

In an equilibrium state, we have  $dS = d(U/T) - \ln z dN$  where  $S$  is the entropy per unit area of the system, and  $U$  is the corresponding internal energy. For the hard rod system at hand, every microscopic configuration has the same energy, hence  $dU = 0$  and  $dS/dN = \ln z$ . It follows that the entropy  $S$  reaches an extremum at  $z = 1$ . That this is a maximum follows from the fact that  $S$  vanishes as  $z \rightarrow 0$ . The reduction of entropy for  $z > 1$  is an outcome of curtailment of placement possibilities due to the hard-core interactions. At much higher values of  $z$ , the equilibrium state develops longer ranged orientational correlations, as will be discussed in section III below.

In our Monte Carlo studies, we adopted the particle based procedure for evaporation and used  $\kappa \equiv \frac{\Gamma_d}{\gamma_e}$  as a control parameter. We varied  $\kappa$  in the range 1 to 40 and monitored the resulting density and orientational correlations. We used an  $L \times L$  substrate (with  $L = 15$  and 25) where  $L$  is in units of needle length. For each value of  $\kappa$  we made multiple runs, allowing up to  $10^7$  Monte Carlo time steps for equilibration. The Monte Carlo time  $t$  is defined as the number of attempts divided by  $L^2$ . Averaging was done over 10 sets of independent runs and 1000 configurations from each run after equilibration. Figure 1(a) shows the variations of the density with  $\kappa$ , while Fig. 1(b) shows  $\rho$  plotted against  $z/a = \rho\kappa$ . The inset in Fig. 1(a) shows a marked change in the dependence of  $\rho/(\kappa - 1)$  on  $\kappa$  for  $\kappa$  in the range 20-25. As we shall see, there is a transition to a phase with power law decay of orientational correlations beyond  $\kappa = \kappa_c \simeq 25$ , as illustrated by the representative configurations shown in Fig. 2 for different values of  $\kappa$ . We will turn to a quantitative study of orientational ordering in the next section.



(a)



(b)

FIG. 1: (a) The variation of  $\rho$  with  $\kappa$  shows a change of behaviour for  $\kappa$  in the range 20-25. This is more prominently depicted in the inset which shows the variation of  $\rho/(\kappa - 1)$ . (b) Variation of  $\rho$  with  $z/a$ . The inset shows the initial portion of the curve.

### III. ORIENTATIONAL ORDERING

#### A. Order parameter

For a system of  $N$  hard rods in 2D, the nematic order parameter  $q$  is given by

$$q = \frac{1}{N} \left\langle \sum_{i=1}^N \cos(2\theta_i) \right\rangle \quad (2)$$

where  $\theta_i$  is the angle made by the  $i^{\text{th}}$  rod with the nematic director, which itself has an orientation  $\phi$  with respect to a fixed reference X-axis. Both  $\phi$  and  $q$  can be found by studying the tensor order parameter defined as

$$\mathbf{Q}_{\alpha\beta} = \frac{1}{N} \left\langle \sum_{i=1}^N [2u_\alpha(i)u_\beta(i) - \delta_{\alpha\beta}] \right\rangle \quad (3)$$

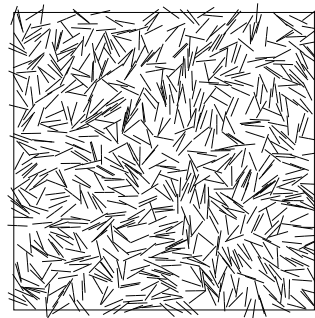
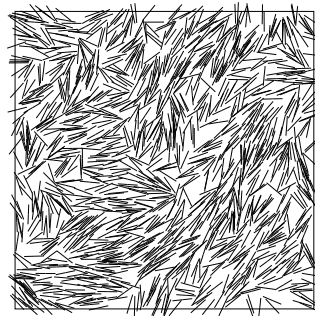
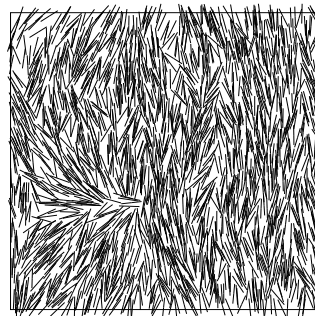
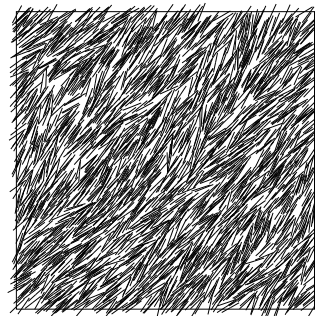
(a)  $\kappa \simeq 19$ (b)  $\kappa \simeq 24$ (c)  $\kappa \simeq 32$ (d)  $\kappa \simeq 39$ 

FIG. 2: Snapshots of hard rod configurations at different values of  $\kappa$ . The substrate size is  $15 \times 15$ . Observe the formation of defects in the configurations (a), (b) and (c).

where  $u_\alpha(i)$  is the  $\alpha^{\text{th}}$  component of  $\mathbf{u}(i)$ , the vector specifying the orientation of the  $i^{\text{th}}$  rod. The eigenvalues of  $\mathbf{Q}_{\alpha\beta}$  are  $\pm q$ , and the corresponding eigenvectors pick out directions along and perpendicular to the director orientation  $\phi$ . Insofar as there is no long range order in the 2D needle system,  $q$  vanishes in the thermodynamic limit. In simulations on finite systems, though,  $q$  may appear to be non-zero (Fig. 2(d)), over short times. Tracking the onset of such an apparent value is not a reliable way to locate the transition point.

### B. Orientational cumulant of $q$

A better indicator of the transition point, and also the nature of the ordered phase, is provided by probability distribution functions  $P_L(s)$  of  $s$ , where  $s$  is the block-averaged value of the local order parameter with the system divided into blocks of finite size  $L$  [21]. At criticality,  $P_L(s)$  approaches a scaled universal form for large  $L$  [21, 22]. A measure of the non-Gaussian character of  $P_L(s)$  is provided by the reduced 4<sup>th</sup> order cumulant of  $s$

$$U_L = 1 - \frac{\langle s^4 \rangle_L}{3\langle s^2 \rangle_L^2} \quad (4)$$

where  $L$  is the linear size of the sub-system (block). We expect  $U_L \rightarrow 0$ , for  $T > T_c$  and  $L \gg \xi$ , while  $U_L \rightarrow U_\infty = 2/3$ , for  $T < T_c$  and  $L \gg \xi$ , where  $\xi$  denotes the correlation length. For  $L \ll \xi$ ,  $U_L$  stays close to a universal fixed point value  $U^*$ . Thus, the occurrence of a critical point with  $\xi = \infty$  can be identified by plotting  $U_L$  against  $T$  for various values of  $L$ , and looking for common intersection point.

We used the cumulant intersection technique to analyse the Monte Carlo data of our model by monitoring  $U_L$  (Eq. 4) using the eigenvalue  $q$  of the tensor of Eq.(3) as a measure of order parameter. The analysis was performed as follows : We simulated a single large system of size  $K \times K$  ( $K = 25$ ) and divided it into subsystems of size  $L \times L$ , thereby having total  $M^2$  number of subsystems with  $M = K/L$  [22]. Then,  $M$  was incremented in integer steps starting from 1 and  $U_L$  was estimated for those subsystem sizes  $L$  where a good analysis is possible. Consequently, we did not consider very small or very large values of  $M$ . Also, the curve for  $M = 12$  lies anomalously low and was not included. The number of subsystems ( $M$ ) we use for estimating the cumulant range from 8 to 20. Fig. (3) shows the variation of  $U_L$  as a function of  $\kappa$  for various values of  $L$ .

The collapse of the cumulant data beyond  $\kappa_c \simeq 25.8$ , seen in Fig. 3 suggests a phase with power-law correlations.

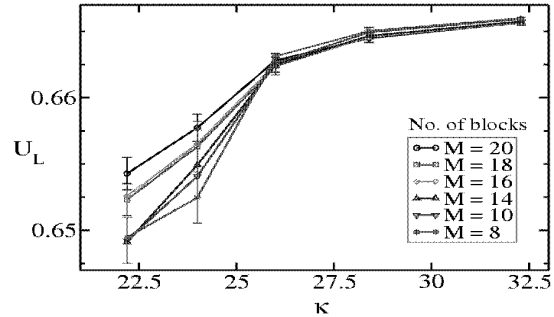


FIG. 3: Orientational cumulants  $U_L$  as a function of deposition-evaporation ratio  $\kappa$  for various subsystem sizes  $L = K/M$ . Note the collapse of the curves beyond  $\kappa_c \simeq 25$ , pointing to the occurrence of a power law phase.

### C. Orientational correlation functions

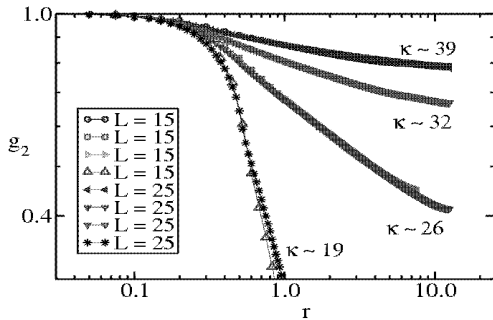
Let us define a general orientational correlation function  $g_\ell(r, t) = \langle \cos[\ell(\theta(r, t) - \theta(0, 0))] \rangle$  where  $\ell$  is an even integer. We studied static and dynamical properties by investigating  $g_\ell(r, 0)$  and  $g_\ell(0, t)$ . We calculated spatial correlations by forming circular bins around each rod in turn, computing  $g_\ell(r, 0)$  for each bin, repeating this process for all rods in the configuration and averaging over all rods (see Fig.4). The dynamical correlation function,  $g_\ell(0, t)$  was calculated by coarse-graining. The system was divided into a number of small cells ( $1 \times 1$ ) and an average value of orientation was assigned to each cell by averaging over the orientations of those needles whose centres of mass lie in the cell. The value of  $g_\ell(0, t)$  was computed using this average value over each time frame, and averaging over all the cells (see Fig.5). The initial drops of the curves in Figs. 4(b) and 5(b) are sensitive to the size of the cell used, while the power laws seen at the larger times do not depend on the cell size.

In the nematic-like phase, i.e. for  $\kappa$  beyond  $\kappa_c$ , the correlations decay algebraically  $g_\ell(r, 0) \sim r^{-\eta_\ell}$  and  $g_\ell(0, t) \sim t^{-\beta_\ell}$ . We found that the values of the exponents  $\eta_\ell$  and  $\beta_\ell$  vary continuously with  $\kappa$  as shown in Table I. The estimations were done over 10 independent sets of configurations, each averaged over 1000 configurations. For  $\kappa \simeq \kappa_c$ , we observed that  $\eta_2 \simeq 0.23 \pm 0.03$  close to the Kosterlitz-Thouless predicted value 0.25. Our results for the static case, agree with those reported by Frenkel and Eppenga [8] in the case of a fixed number of hard rods on 2D plane. We confirm that at the critical point  $\kappa = \kappa_c$ , the mean density is  $\simeq 7$  [8].

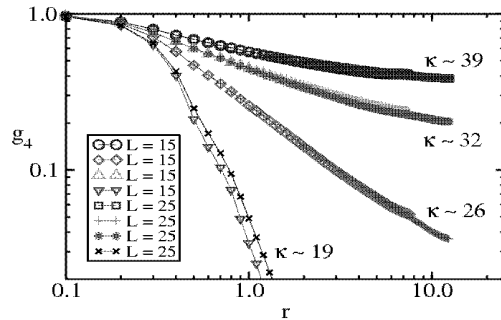
For  $\kappa > \kappa_c$ , it was observed that exponents obtained from static correlations  $g_2(r)$  and  $g_4(r)$  are related through  $\eta_2 \simeq \eta_4/4$ . It was also found that the exponents derived from the temporal correlations  $g_2(t)$  and  $g_4(t)$  are related in a similar way, i.e.  $\beta_2 \simeq \beta_4/4$ . Further, the ratios  $\eta_\ell/\beta_\ell \simeq 2.0$  for  $\ell = 2$  and 4, implying that the dynamical exponent  $z_{dyn}$  is 2. These observations can be

TABLE I:  $\kappa$  dependence of exponents  $\eta_\ell$  and  $\beta_\ell$  for  $\ell = 2$  and  $4$ . The estimated error is indicated in the brackets.

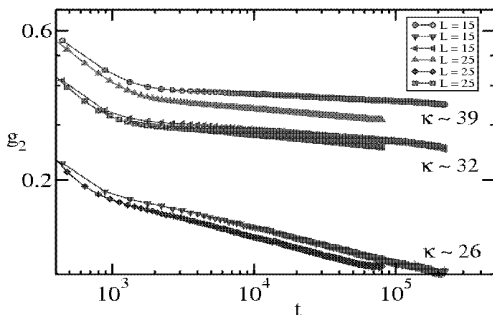
$\kappa$	$\rho$	$\eta_2$	$\eta_4$	$\beta_2$	$\beta_4$	$K/B$
26.0	7.3	0.23 (0.03)	0.87 (0.06)	0.11 (0.04)	0.31 (0.06)	$5.3 \times 10^{-3}$
32.3	9.4	0.098 (0.006)	0.41 (0.02)	0.037 (0.007)	0.16 (0.04)	$12.8 \times 10^{-3}$
39.0	11.4	0.059 (0.003)	0.25 (0.01)	0.022 (0.003)	0.09 (0.01)	$21.4 \times 10^{-3}$



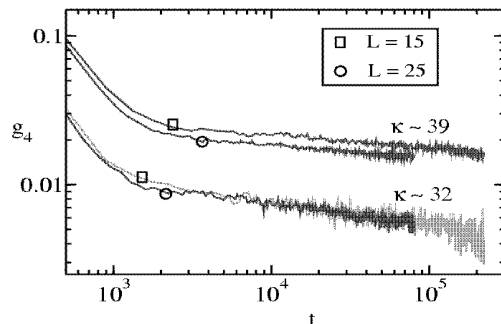
(a)



(a)



(b)



(b)

FIG. 4: Log-log plots of (a)  $g_2(r, 0) = \langle \cos[2(\theta(r, t) - \theta(0, t))] \rangle$  and (b)  $g_2(0, t) = \langle \cos[2(\theta(r, t) - \theta(r, 0))] \rangle$  showing the static and temporal behaviour respectively of  $g_2(r, t)$ . Data is shown for systems of sizes  $15 \times 15$  and  $25 \times 25$ , and different values of  $\kappa$ .

FIG. 5: Log-log plots of (a)  $g_4(r, 0) = \langle \cos[4(\theta(r, t) - \theta(0, t))] \rangle$  and (b)  $g_4(0, t) = \langle \cos[4(\theta(r, t) - \theta(r, 0))] \rangle$  showing the static and temporal behaviour respectively of  $g_4(r, t)$ , for the same system sizes and values of  $\kappa$  as in Fig. 4.

understood on the basis of the simple model discussed below.

In order to model the dynamics we note that the stochastic evaporation and deposition events change the local value of the coarse-grained angle field  $\theta$  in a noisy, diffusive way. In the discussion below, we take the angle to be an unconstrained variable running from  $-\infty$  to

$+\infty$  with  $(\theta + n\pi)$  denoting the same needle orientation for integer  $n$ . We consider a simple phenomenological equation

$$\frac{\partial \theta}{\partial t} = K \nabla^2 \theta + \xi \quad (5)$$

where  $\xi$  denotes white noise which satisfies

$$\langle \xi(\mathbf{r}, t) \xi(\mathbf{r}', t') \rangle = B \delta(\mathbf{r} - \mathbf{r}') \delta(t - t') \quad (6)$$

where  $B$  is a constant. This is of the same form as the Edwards-Wilkinson equation [23], which describes the evolution of a fluctuating interface. In our context, Eq.(5) follows from the symmetric form of the Frank free energy  $F = \frac{1}{2} K \int (\nabla\theta)^2 d\theta$  on using the phenomenological Langevin equation  $\frac{\partial\theta}{\partial t} = \frac{-\delta F}{\delta\theta} + \xi$ . A more complete description would involve coupled equations for the non-conserved density and orientational fields. From Eq.(5) and (6) it follows that

$$\langle\theta(\mathbf{r} + \mathbf{r}', t + t')\theta(\mathbf{r}, t)\rangle = \frac{B}{64\pi^5 K} \int \frac{d^2k}{k^2} e^{i\mathbf{k}\cdot\mathbf{r}'} e^{-Kk^2 t'} \quad (7)$$

Setting  $t' = 0$  we find that

$$\langle[\theta(\mathbf{r} + \mathbf{r}', t) - \theta(\mathbf{r}, t)]^2\rangle = \frac{B}{32\pi^5 K} \times 2\pi \ln(r) \quad (8)$$

which, using the Gaussian property of  $\theta$ , further implies

$$\langle\cos\{\ell[\theta(\mathbf{r} + \mathbf{r}', t) - \theta(\mathbf{r}, t)]\}\rangle \simeq r^{-\eta_\ell} \quad (9)$$

where  $\eta_\ell = \ell^2 B / 32\pi^4 K$ . The measured values of  $\eta_\ell$  can be used to find  $K/B$ , whose value is included in Table I.

Similarly, setting  $r' = 0$  in Eq.(7) we find the autocorrelation function

$$\langle\cos\{\ell[\theta(\mathbf{r}, t + t') - \theta(\mathbf{r}, t)]\}\rangle \simeq t^{-\beta_\ell} \quad (10)$$

where  $\beta_\ell = \ell^2 B / 64\pi^4 K$ . Thus, for all  $\kappa > \kappa_c$  the ratio of  $\eta_4$  to  $\eta_2$  (and  $\beta_4$  to  $\beta_2$ ) is expected to be 4; as we have seen above, our numerical results confirm this. Also, we find the dynamical exponent  $z_{dyn} = \eta_\ell / \beta_\ell$  is  $\simeq 2.0$ .

#### IV. EFFECT OF INHOMOGENEOUS $\kappa$

In this section, we explore the effects of having a spatial variation of the deposition-evaporation rate ratio  $\kappa$ . In a physical system such a variation could arise from the variation of substrate temperature from one spot to another as the local temperature would influence the local detachment rate. As expected, such changes induce a spatial variation of the density; more interestingly, they turn out to have a strong effect on the orientational order as well. We explore these effects by considering several types of spatial variations of  $\kappa$ .

In parallel to the discussion in section II, let  $\Gamma_d(x)$  and  $\gamma_e(x)$  denote the deposition and evaporation rates at small elements of area  $a$  centered at point  $x$  in the plane, and let  $\kappa(x) = \frac{\Gamma_d(x)}{\gamma_e(x)}$ . Let  $C'$  be the configuration reached from configuration  $C$  by removing the rod at  $x_m$  and let  $P(C')$  and  $P(C)$  be the weights of the respective configurations in steady state. We can check that the condition of detailed balance is valid when  $P(C)$  has the product form  $P(C) = \prod_i z(x_i)$  where  $z(x_i) = a\rho(x_i)\kappa(x_i)$  is the local fugacity at the location of the centre of mass of the  $i^{th}$  rod. If  $C'$  is obtained from  $C$  by evaporating the  $m^{th}$  rod, then evidently  $P(C) = P(C') \times z(x_m)$ . Recalling

that  $W(C) = a\Gamma_d(x_m)$  and  $W(C') = \Gamma_e^a(x_m)$ , we see that the condition of detailed balance is valid.

Thus the system reaches an equilibrium steady state which, however, is inhomogeneous in density, due to the non-uniform position dependence of  $\kappa$ . The nature of orientational order depends strongly on the way in which  $\kappa$  is specified to vary over the plane. Below we consider several types of variations

(i) A single interface separating low and high  $\kappa$  regions,

$$\begin{aligned} \kappa(x) &= \kappa_1, \text{ for } x < \frac{L}{2}, \\ \kappa(x) &= \kappa_2, \text{ for } x > \frac{L}{2}. \end{aligned}$$

(ii) A uniform gradient in  $\kappa$  across the substrate,

$$\kappa(x) = \kappa_1 \left(1 + \alpha \frac{x}{L}\right)$$

(iii) Random variation of  $\kappa$  in the X-direction only,

$$\kappa(x) = \kappa_1 + \delta\kappa(x)$$

where  $\delta\kappa(x) < \kappa_1$  is a random function of  $x$ .

(iv) A random binary assignment of  $\kappa$  on a grid on the 2D substrate

In the first three cases, periodic boundary conditions were applied in Y-direction and open boundary conditions along X. In the last case, open boundaries were used in both directions. In all the cases considered, the ranges of  $\kappa$  values were chosen to be above  $\kappa_c$ , the critical value in the uniform case. Our findings are as follows :

##### A. $\kappa_1 - \kappa_2$ interface

Here, a uniform value  $\kappa_1$  operates upto half-way across the 2D plane along the X-direction, while  $\kappa = \kappa_2 (> \kappa_1)$  in the remaining half. In the vicinity of the interfacial region, the rods are observed to orient in the direction of the  $\kappa$  gradient i.e. perpendicular to the interface (see Fig. 6(a)).

This can be understood on entropic grounds. That arrangement of rods is favoured which maximizes the entropy. By symmetry, the preferred average orientation of rods should be either (a) parallel or (b) perpendicular to the interface. Consider these rods in the high- $\kappa$  half, whose centres lie very close to the interface (within half a rod length) so that part of such rods can reach into the low density side. Small variations in the angle of each rod would contribute to the entropy, but these are limited by the presence of other rods. A horizontal average alignment allows the rods to sample a less dense environment, and thus be subject to fewer constraints, on one side. Thus, option (b) would be preferred over (a).

In fact, this effect should also lead to rods getting aligned horizontally, if they are close to an open boundary. This can be seen in Fig. 6(b), which shows a system with uniform  $\kappa$  and open boundary conditions along the X-direction. The alignment is similar to that is a simple model of needles on a 1-d substrate discussed in the Appendix A.

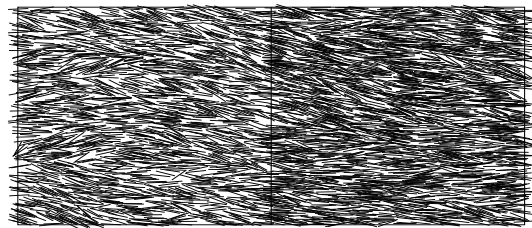
Returning to the  $\kappa_1 - \kappa_2$  system, the effect of interface-induced horizontal alignment is felt for some distance away from the interface on both sides. This is evident in Fig. 6(a), which shows a steady state configuration in a system of size  $25 \times 15$  (in units of rod length), with  $\kappa_1 = 27$  and  $\kappa_2 = 50$ . We also considered a case where there are two interfaces (Fig. 6(c)). The figure shows a  $80 \times 15$ -sized system divided into left and right quarters with  $\kappa = 27$ , while the middle half has  $\kappa = 50$ . This construction allows periodic boundary conditions in both the directions. Evidently, this system with two interfaces shows horizontal alignment, independent of any kind of boundary effect. However, for a large enough size, the system reverts to a power-law phase in the region far from the interface as observed in the uniform  $\kappa$  case. The correlation function decays as a power of distance away from the interface, as shown in Fig. 6(d).

## B. Uniform $\kappa$ gradient

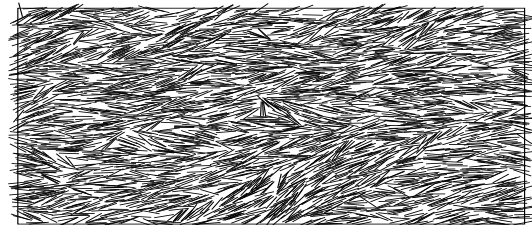
This case is related to the case discussed above, as the linear increase in  $\kappa$  may be viewed as a continuous succession of interfaces from one end to the other. Since each interface induces an alignment of rods across it, this results in overall alignment of the rods in the system (see Fig. 7). Note that the alignment is not an outcome of spontaneous breaking of orientational symmetry, as the gradient in  $\kappa$  singles out a direction in space. We checked that the horizontal alignment is not tied to the aspect ratio of the container by simulating a system size  $10 \times 40$ , and observing overall horizontal alignment of rods in the steady state.

Figure 7 shows a steady state configuration in a system of size  $25 \times 15$ , with  $\kappa$  varying linearly from a value  $\kappa_L = 32$  at the left end to a value  $\kappa_R = 50$  at the right end. In our simulations, the system was equilibrated for  $10^7$  MCS and  $10^4$  post-equilibration configurations were used to calculate averages. We studied the spatial and dynamical behaviour of the orientational correlation function  $g_2(r, t) = \langle \cos[2(\theta(r, t) - \theta(0, 0))] \rangle$ . Since the system is inhomogeneous along the X-direction, the substrate was divided into vertical strips, each having width of a rod length, and each strip was studied separately. The Y-density of needles inside each strip was uniform though the density varies from strip to strip. We monitored the correlation function  $g_2(y) = \langle \cos[2(\theta(y + y_0) - \theta(y_0))] \rangle$  (see Fig. 8), and found that  $g_2(y)$  decays exponentially to a non-vanishing constant value  $q_0$  which differs from strip to strip. For the system under study,  $q_0^2$  varies in the range 0.68-0.77 over the strips.

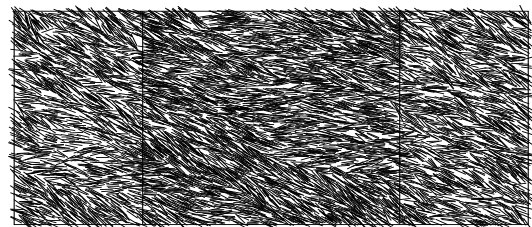
The dynamical correlation function, i.e.  $g_2(t) = \langle \cos[2(\theta(t) - \theta(0))] \rangle$  was calculated by coarse-graining. The system was divided into number of small cells ( $2 \times 2$ ) and an average value of orientation was assigned to each cell by averaging over needles in it. The plot of  $g_2(t)$  is shown in Fig. 9 for cells at different values of X. Each curve shows an exponential approach to a non-zero con-



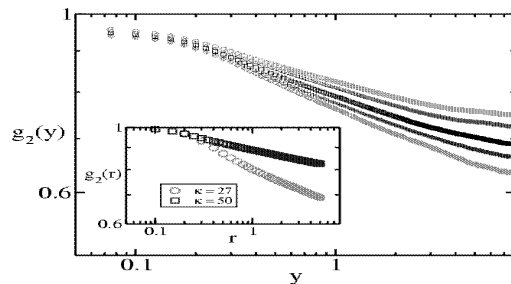
(a)



(b)



(c)



(d)

FIG. 6: (a) Snapshot of a typical hard rod configuration with a single  $\kappa_1 - \kappa_2$  interface. The system size is  $25 \times 15$  and  $\kappa_1 = 27$  (left half) and  $\kappa_2 = 50$  (right half). Notice the difference in density in the two halves. (b) A typical configuration of size  $25 \times 15$  with uniform  $\kappa$  and open boundary conditions along the X-direction. (c) A dual-interface configuration of  $80 \times 15$ -sized system. The middle half of size  $40 \times 15$  and with  $\kappa = 50$  separates two quarters, each of size  $20 \times 15$  and having  $\kappa$  value 27. This construct allows use of periodic boundary conditions in both the directions. (d) This plot shows the decay of the orientational correlation function  $g_2(\mathbf{y}) = \langle \cos[2(\theta(\mathbf{y}) - \theta(0))] \rangle$  calculated for a pair of points in the same vertical strip of unit width. Curves from bottom to top correspond to different strips with increasing  $\kappa$  in the configuration (a). The inset shows  $g_2(\mathbf{r}) = \langle \cos[2(\theta(\mathbf{r}) - \theta(0))] \rangle$  measured radially for a box of size  $6 \times 6$  which is positioned at the centre of each of the left and right halves of the same configuration.

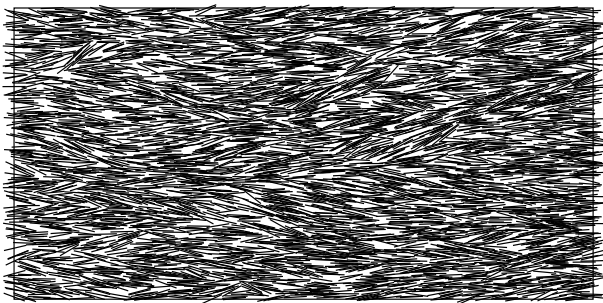


FIG. 7: A typical configuration for a  $25 \times 15$ -sized system with a uniform  $\kappa$  gradient, with  $\kappa_L = 32$  and  $\kappa_R = 50$  at the two ends respectively. The horizontal alignment induced by the gradient is evident.

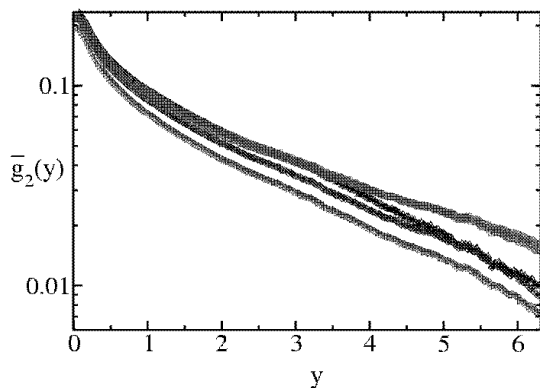


FIG. 8: Correlation function in a  $25 \times 15$ -sized system with a uniform  $\kappa$  gradient. Shown is the log-normal plot  $\bar{g}_2(y) = \langle \cos[2(\theta(y) - \theta(0))] \rangle - q_0^2$  for pairs of points in the same vertical strip of unit width. Curves from bottom to top correspond to different vertical strips in the order of increasing  $\kappa$ . It is evident from the plots that  $\bar{g}_2(y)$  exhibits exponential decay.

stant value. The behaviour of both the spatial and dynamical orientational parts of the correlation functions indicates a phase with overall orientational alignment.

### C. Random variation of $\kappa(x)$

If  $\kappa$  varies randomly (with  $\kappa > \kappa_c$ ) along the X-direction but is uniform along Y, the resulting state once again exhibits horizontal alignment with needles aligned along the X-direction. The gradient in  $\kappa$  is randomly fluctuating, both in magnitude and sign, but is along the X-direction; and can once again be viewed as continuous succession of interfaces. As with the constant gradient case, the result is a state with overall alignment.

Figure 10 shows a steady state configuration obtained with a quenched random variation of  $\kappa(x)$ . The system was simulated by varying  $\kappa$  randomly around a value of  $\kappa$  such that  $\kappa \pm \delta\kappa(x) > \kappa_c$ , where  $\delta\kappa(x)$  denotes ran-

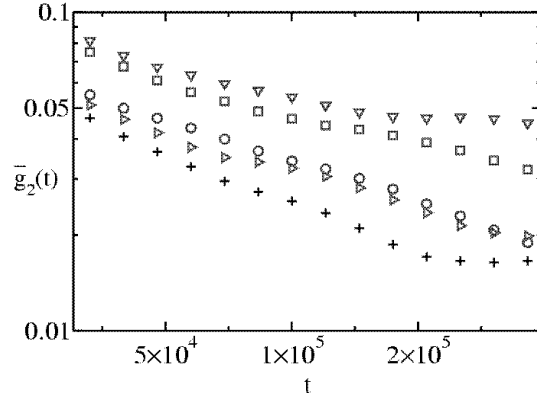


FIG. 9: Dynamical correlation function in the system of Fig. 7 and 8. Log-normal plots of  $\bar{g}_2(t) = \langle \cos[2(\theta(t) - \theta(0))] \rangle - q_0^2$  as shown, with curves from bottom to top correspond to different cells with increasing  $\kappa$  (refer to the main text for details).

dom variations along X-direction. We used  $\kappa \simeq 32$  and  $\delta\kappa = 2.0$ . The correlation functions  $g_2(y)$  and  $g_2(t)$  behave similarly to the uniform gradient case (see Fig. 11 and 12). Thus, this case also yields a phase with overall orientational alignment.

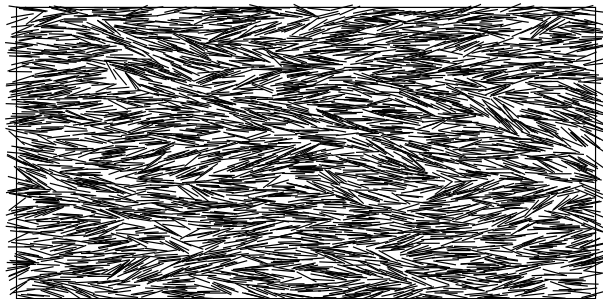


FIG. 10: A typical configuration for a  $25 \times 15$ -sized system with a  $\kappa$  gradient achieved by varying the value of  $\kappa$  randomly around 32 in the X-direction only. The horizontal alignment induced by the gradient is evident.

### D. 2D random binary distribution of $\kappa$ values

In this case, the fugacity is set inhomogeneously in a quenched disordered fashion, so that the tendency to align locally along gradients results in competing patterns of order, i.e the system is frustrated. The resulting state has glassy features and contains domains of different orientations (see Fig. 13) [24].

In our simulations, we divided the substrate of size  $25 \times 25$  into a grid of unit length squares. Each square was randomly assigned a  $\kappa$  value either 27 or 50 (both greater than  $\kappa_c$ ). The random  $\kappa$  gradient across square edges generates local disorder, which can disrupt the ori-

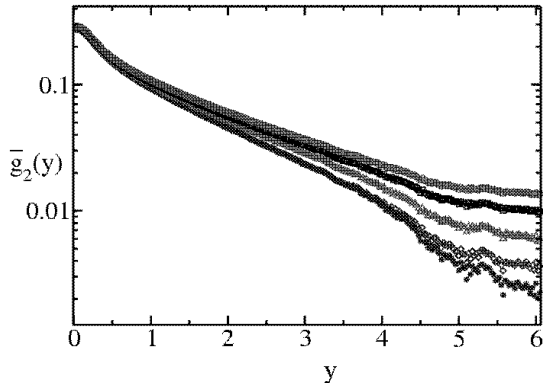


FIG. 11: Correlation function in a  $25 \times 15$ -sized system with a random  $\kappa$  gradient in the X-direction only. Shown is the log-normal plot  $\bar{g}_2(y) = \langle \cos[2(\theta(y) - \theta(0))] \rangle - q_0^2$  for pairs of points in the same vertical strip of unit width. Curves from bottom to top correspond to different vertical strips in the order of increasing  $\kappa$ . It is evident from the plots that  $\bar{g}_2(y)$  exhibits exponential decay.

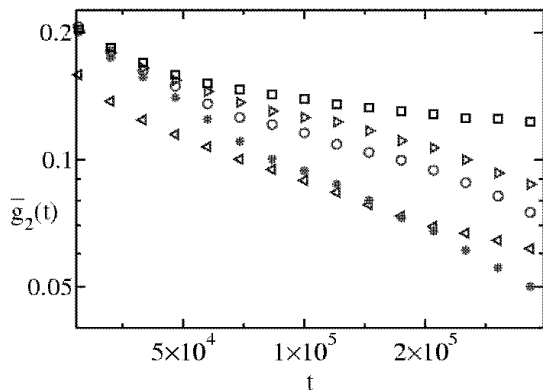
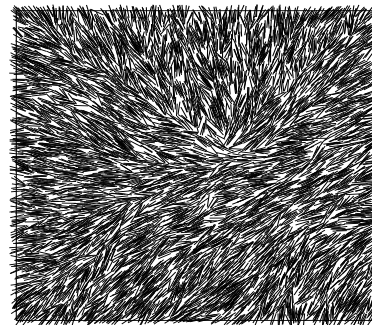


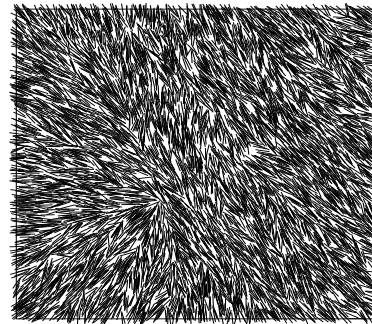
FIG. 12: Dynamical correlation function in the system of Fig. 10 and 11. Log-normal plots of  $\bar{g}_2(t) = \langle \cos[2(\theta(t) - \theta(0))] \rangle - q_0^2$  as shown, with curves from bottom to top correspond to different cells with increasing  $\kappa$ .

entational order and result in destruction of orientational alignment on the scale of the system size. The effect of quenched random disorder due to orientational randomness of cross-links in a system of nematic elastomers has been studied earlier [25] and the model was reported to have spin-glass like behaviour. In our model, the disorder emerges from the randomness in the spatial distribution of  $\kappa$  values. We find that the spatial correlation  $g_2(r)$  decays exponentially to zero (Fig. 14) whereas the dynamical part  $g_2(t)$  seems to decay in an algebraic manner to a non-zero value (Fig. 15).

The behavior is suggestive of a glassy system which is disordered in space but relaxes slowly in time. More-



(a)



(b)

FIG. 13: Snapshots of hard rod configurations for random binary distribution of  $\kappa$  values 27 and 50 on the substrate of size  $25 \times 25$ . Representative configurations characterizing two different states ((a) and (b)) which are reached from different initial conditions, for the same  $\kappa$  distribution.

over, it was also found that with same quenched disorder arrangement, different initial conditions lead to different states. Typical configurations in each of these states are shown in Fig. 13, which is a glass-like feature.

## V. CONTINUUM DESCRIPTION

We have seen that spatial inhomogeneities in deposition or evaporation rates induce interesting orientational patterns in the system of hard needles. We now turn to a discussion of the effects of such inhomogeneities within a continuum description [26]. On a large length scale, we expect the properties of the system with uniform  $\kappa$  to be governed by the Frank free energy, which, for a two

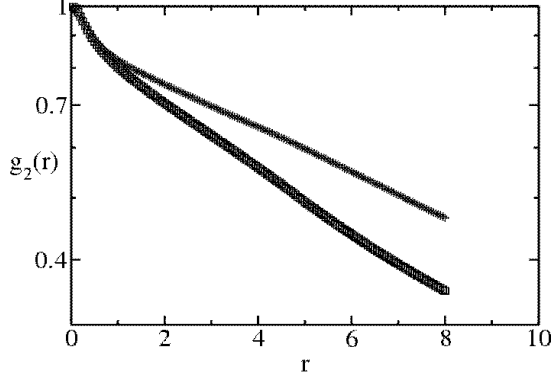


FIG. 14: Evidence for exponential decay of spatial correlations in a system with random binary distribution of  $\kappa$ . The figure shows log-normal plots of  $g_2(\mathbf{r}) = \langle \cos[2(\theta(\mathbf{r}) - \theta(0))] \rangle$ . The parameters are the same as in Fig. 13, and the curves correspond to the different steady states evolved from two different initial conditions.

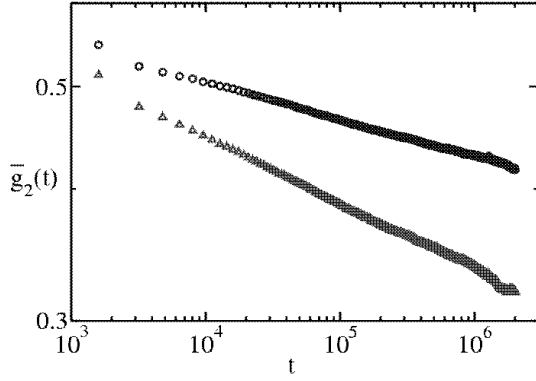


FIG. 15: Evidence for a power law decay of temporal correlations in a system with random binary distribution of  $\kappa$ . The figure shows log-log plots of  $\bar{g}_2(t) = \langle \cos[2(\theta(t) - \theta(0))] \rangle - q_0^2$ . The parameters are the same as in Fig. 13, and the curves are obtained in the different steady states reached from two different initial conditions.

dimensional system, can be written as

$$F_K = \int d^2r \left[ \frac{K_1}{2} (\nabla \cdot \hat{n})^2 + \frac{K_3}{2} (\hat{n} \times (\nabla \times \hat{n}))^2 \right] \quad (11)$$

The two terms describe, respectively, contributions of splay and bend to the free energy; there is no contribution from twist in 2-d. If  $K_1 = K_3$ ,  $F_K$  reduces to the isotropic form  $\frac{1}{2} \int d^2r K (\nabla \phi)^2$ .

Inhomogeneities in deposition-evaporation rates lead to the occurrence of spatial gradients  $\nabla \kappa$ , which lead to further terms in the free energy. The form of these terms can be written down by constructing scalars involving  $\nabla \kappa$

and  $\hat{n}$ , and respecting invariance under  $\hat{n} \leftrightarrow -\hat{n}$ . Two important sets of terms are

$$F_J = \int d^2r \frac{J_1}{2} [(\nabla \kappa \cdot \hat{n})^2] + \int d^2r \frac{J_3}{2} [(\hat{n} \times (\nabla \kappa \times \hat{n}))^2] \quad (12)$$

and

$$F_L = \int d^2r \frac{L_1}{2} \nabla \kappa \cdot [\hat{n} (\nabla \cdot \hat{n})] + \int d^2r \frac{L_3}{2} \nabla \kappa \cdot [(\hat{n} \cdot \nabla) \hat{n}] \quad (13)$$

The terms in Eqs. (12) and (13) are of second and first order in  $\nabla \kappa$  respectively. The problem is then to minimize  $F_K + F_J + F_L$  for a given space-dependence of the deposition-evaporation ratio  $\kappa(r)$ , and for a given set of coupling constants. Symmetry considerations do not suffice to determine  $K_1, K_2, J_1, J_2, L_1$  and  $L_2$ ; moreover each of these coupling constants could be a function of  $\rho$  which itself can vary in space.

We may obtain the form of these gradient-induced terms in the free energy and their density dependences from the observation that the most direct consequence of a change in  $\kappa$  is to induce a change in density, thereby influencing the elastic energy. To incorporate this effect, we insert a density dependence in the Frank free energy by replacing  $\hat{n}$  in Eq. (11) by  $(\rho(r)\hat{n}/\rho_0)$  where  $\rho(r)$  and  $\rho_0$  are the local and average densities respectively. The resulting form of the free energy  $F_\rho$  is described in Appendix B, where the correspondence with terms in  $F_K, F_J$  and  $F_L$  is also discussed.

Let us now turn to the consequences of the new terms. First consider a spatial gradient which is uniform,  $\nabla \kappa = \alpha \hat{x}$  (case (ii) above). Before turning to the minimization of full free energy, it is useful to consider the effects of two terms at a time to get an idea of their consequences. To this end, first consider  $F_K + F_J$ . Evidently,  $F_K$  is minimized by any arrangement in which  $\hat{n}$  is uniform in space. Writing  $\hat{n} = \hat{x} \cos \phi + \hat{y} \sin \phi$ , we find

$$F_J = \alpha^2 (J_1 \cos^2 \phi + J_3 \sin^2 \phi). \quad (14)$$

If  $J_3 > J_1$ , the free energy  $F_K + F_J$  is minimized by having  $\phi = 0$ , i.e. a state with alignment along the direction of the gradient. Our numerical results, supported by the entropic considerations given above, show alignment in the direction of the gradient and thus imply that  $\Delta J \equiv J_3 - J_1 > 0$ .

Now consider  $F_K + F_L$ . Setting  $\nabla \kappa = \alpha \hat{x}$  in Eq. (13), we find

$$F_L = -\alpha(L_1 + L_3) \sin \phi \cos \phi \frac{\partial \phi}{\partial x} + \alpha(L_1 \cos^2 \phi - L_3 \sin^2 \phi) \frac{\partial \phi}{\partial y} \quad (15)$$

The minimization of the sum of the gradient terms ( $F_K + F_L$ ) is accomplished straightforwardly on noting that each of the  $L_1$  and  $L_3$  terms is an eigenfunction of

the Frank elastic matrix. The result of the minimization is

$$\frac{\partial\phi}{\partial y} = \frac{-L_1}{K_1}\cos^2\phi + \frac{L_3}{K_3}\sin^2\phi \quad (16)$$

$$\frac{\partial\phi}{\partial x} = \left(\frac{L_1}{K_1} + \frac{L_3}{K_3}\right) \cos\phi \sin\phi \quad (17)$$

These terms describe a spiralling tendency of the director in space.

However, the full problem involves minimizing  $F_J + F_K + F_L$ . Let us assume  $F_J$  to be dominant so that the director is primarily aligned along the gradient, i.e.  $\Delta J$  is large implying  $\phi$  is small. In this case, Eqs.(14) and (15) imply  $\partial\phi/\partial y \approx -L_1/K_1$  which describes a tendency of the director to fan out in a spiral. However, large angles are curbed by  $F_J$  which would penalize angle excursions beyond  $\phi_0 \propto \frac{1}{\sqrt{\Delta J}}$ . Typical configurations are thus likely to contain bunches of local splay structures, each with a small opening angle  $2\phi_0$ . The opening angle would be expected to fall as the magnitude of the gradient  $\alpha$  is increased. We have not made a systematic study of this effect, but we did observe that the average opening angle is smaller on the high- $\kappa$  end – a consequence of the density dependence of the coupling constants, discussed in Appendix B.

For case (iii) in which  $\kappa(x)$  varies randomly, we see that  $F_J = \overline{\alpha^2}(J_1\cos^2\phi + J_3\sin^2\phi)$  where  $\overline{\alpha^2}$  is the spatial average of the mean squared gradient. As for case (ii), the free energy is minimized by having a state with alignment along the gradient, provided  $J_3 > J_1$ .

In case (iv), the gradients that appear in Eq. (12) are random in direction leading to frustration in the arrangement of needles. In view of the non-uniformity induced by  $F_J$ , the gradient terms  $F_K$  and  $F_L$  would play an important role. An analytic characterization of the glassy state that results is not attempted here, but Eqs.(11), (12) and (13), supplemented by Appendix B would provide a starting point for a theoretical description.

## ACKNOWLEDGMENTS

We acknowledge very useful discussions with Yashodhan Hatwalne, Sriram Ramaswamy and Gautam Menon. We thank Deepak Dhar for a critical reading of the manuscript and suggestions.

## APPENDIX A

Motivated by the observed alignment of needles perpendicular to the  $\kappa_1 - \kappa_2$  interface in section IV A, we

introduce and investigate orientational order in a simple model of deposition-evaporation dynamics of needles on a 1-d substrate. During deposition, attempts are made at rate  $\Gamma_d$  to add needles to the substrate such that their centres lie on the line. The centre of mass coordinates and orientation of each needle are chosen randomly; any event resulting in overlap with earlier deposited needles is discarded. Simultaneously, needles chosen randomly from those present are removed (evaporated). Periodic boundary conditions are applied.

The system reaches an equilibrium steady state with a density depending on the ratio  $\kappa$  of deposition and evaporation rates (Fig. 16).

We observe that for any density, the needles orient preferentially perpendicular to the 1-d substrate (Fig. 17) implying a non-zero value of the orientational order parameter across the system. A preferred perpendicular orientation allows the needles to achieve better packing. For a fixed density, if the mean orientation of the director is perpendicular to the substrate, needles have the largest leeway to make angular excursions about the mean - i.e. the rotational entropy is then the largest. Fig. 16 shows the variation of the order parameter  $q = \langle \cos 2\phi \rangle$  with  $\kappa$  where  $\phi$  is the angle made with the direction perpendicular to the line.

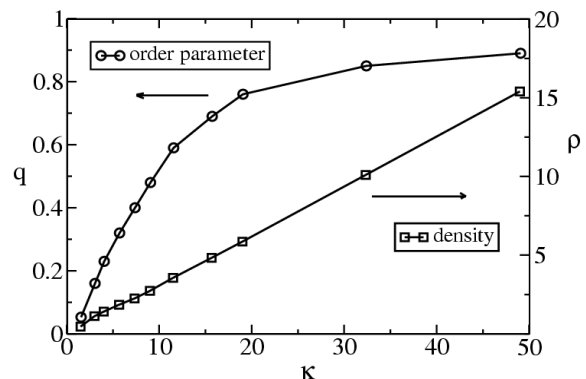


FIG. 16: Variation of the density( $\rho$ ) and order parameter( $q$ ) with  $\kappa$ .

The 1-d model studied here has certain points in common with 2-d models with different values of  $\kappa$  across a line, e.g. the models discussed in section IV. The density in these models is higher on one side than the other, unlike in the 1-d model. Nevertheless the occurrence of an orientationally ordered state which is an outcome of the maximization the entropy of small orientational fluctuations is common to both the situations.

## APPENDIX B

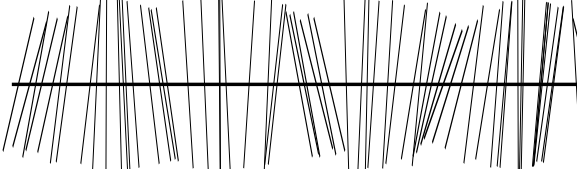


FIG. 17: A portion of a typical configuration with needles on a 1D substrate for  $\kappa = 16$ .

To incorporate the effect of density in the free energy, we write  $(\rho(r)\hat{n}/\rho_0)$  in place of the director  $\hat{n}$  in the Frank free energy  $F_K$  of Eq. (11). The resulting expression  $F_\rho$  for the free energy can be written as

$$F_\rho = \int d^2r \left[ \frac{K_1}{2\rho_0^2} (\nabla \cdot \rho\hat{n})^2 + \frac{K_3}{2\rho_0^4} (\rho\hat{n} \times (\nabla \times \rho\hat{n}))^2 \right] \quad (18)$$

The complete expansion of the integrand involves ten terms as follows :

$$\begin{aligned} & \left[ \frac{K_1}{2\rho_0^2} \rho^2 \sin^2\phi + \left( \frac{K_3}{2\rho_0^4} \rho^2 \right) \rho^2 \cos^2\phi \right] (\partial\phi/\partial x)^2 \\ & + \left[ \frac{K_1}{2\rho_0^2} \rho^2 \cos^2\phi + \left( \frac{K_3}{2\rho_0^4} \rho^2 \right) \rho^2 \sin^2\phi \right] (\partial\phi/\partial y)^2 \\ & + \left[ \frac{K_1}{2\rho_0^2} \cos^2\phi + \left( \frac{K_3}{2\rho_0^4} \rho^2 \right) \sin^2\phi \right] (\partial\rho/\partial x)^2 \\ & + \left[ \frac{K_1}{2\rho_0^2} \sin^2\phi + \left( \frac{K_3}{2\rho_0^4} \rho^2 \right) \cos^2\phi \right] (\partial\rho/\partial y)^2 \\ & + \left[ \frac{-K_1}{2\rho_0^2} + \left( \frac{K_3}{2\rho_0^4} \rho^2 \right) \right] 2\rho \sin\phi \cos\phi (\partial\phi/\partial x) (\partial\rho/\partial x) \end{aligned}$$

$$\begin{aligned} & + \left[ \frac{K_1}{2\rho_0^2} - \left( \frac{K_3}{2\rho_0^4} \rho^2 \right) \right] 2\rho \sin\phi \cos\phi (\partial\phi/\partial y) (\partial\rho/\partial y) \\ & + \left[ \frac{K_1}{2\rho_0^2} - \left( \frac{K_3}{2\rho_0^4} \rho^2 \right) \right] 2 \sin\phi \cos\phi (\partial\rho/\partial x) (\partial\rho/\partial y) \\ & + \left[ \frac{-K_1}{2\rho_0^2} + \left( \frac{K_3}{2\rho_0^4} \rho^2 \right) \right] 2\rho^2 \sin\phi \cos\phi (\partial\phi/\partial x) (\partial\phi/\partial y) \\ & + \left[ \frac{-K_1}{2\rho_0^2} \sin^2\phi - \left( \frac{K_3}{2\rho_0^4} \rho^2 \right) \cos^2\phi \right] 2\rho (\partial\phi/\partial x) (\partial\rho/\partial y) \\ & + \left[ \frac{K_1}{2\rho_0^2} \cos^2\phi + \left( \frac{K_3}{2\rho_0^4} \rho^2 \right) \sin^2\phi \right] 2\rho (\partial\rho/\partial x) (\partial\phi/\partial y) \end{aligned}$$

In case (ii) where  $\kappa$  varies linearly with  $x$ , the density gradient is non-zero only along the X-direction, and vanishes along Y, so the terms involving  $\partial\rho/\partial y$  do not contribute.

We can then read off the density dependence induced in the elastic constants in terms of the original Frank's constants as

$$K'_1(\rho) = \frac{K_1}{\rho_0^2} \rho^2 \quad \text{and} \quad K'_3(\rho) = \frac{K_3}{\rho_0^4} \rho^4$$

Now, comparing the third term with expression with Eq. (14) and writing  $\partial\rho/\partial x = \alpha\zeta(\rho)$  where  $\zeta(\rho) = \partial\rho/\partial\kappa$ , we have

$$J_1(\rho) = \frac{K_1}{\rho_0^2} (\zeta(\rho))^2 \quad ; \quad J_3(\rho) = \frac{K_3}{\rho_0^4} \rho^2 (\zeta(\rho))^2 \quad (19)$$

Similarly, grouping the fifth and the tenth terms together and comparing with Eq. (15), we obtain

$$L_1(\rho) = \frac{K_1}{\rho_0^2} 2\rho\zeta(\rho) \quad ; \quad L_3(\rho) = \left( -\frac{K_3}{\rho_0^4} \rho^2 \right) 2\rho\zeta(\rho). \quad (20)$$

- 
- [1] S. Fraden et al, Phys. Rev. Lett., **63**, 2068 (1989).  
[2] P. G. de Gennes and J. Prost, *The Physics of Liquid Crystals*, 2<sup>nd</sup> Ed. (Clarendon, Oxford, 1993).  
[3] M. F. Islam et al, Phys. Rev. Lett., **92**, 088303 (2004).  
[4] J. A. Cuesta and D. Frenkel, Phys. Rev. A, **42**, 2126 (1990).  
[5] A. Stroobants, H. N. W. Lekkerkerker and D. Frenkel, Phys. Rev. A, **36**, 2929 (1987).  
[6] M. A. Bates and D. Frenkel, J. Chem. Phys. **112**, 10034 (2000).  
[7] M. C. Lagomarsino, M. Dogterom and M. Dijkstra, J. Chem. Phys. **119**, 3535 (2003).  
[8] D. Frenkel and R. Eppenga, Phys. Rev. A, **31**, 1776 (1985).  
[9] J. W. Evans, Rev. Mod. Phys. **65**, 1281 (1993).  
[10] E. Frey and A. Vilfan, Chem. Phys. **284**, 287 (2002).  
[11] V. Narayan, N. Menon and S. Ramaswamy (unpublished).  
[12] R. B. Stinchcombe, M. D. Grynberg and M. Barma, Phys. Rev. E **47**, 4018 (1993).  
[13] P. L. Krapivsky and E. Ben-Naim, J. Chem. Phys. **100**, 6778 (1994).  
[14] A. J. Kolan, E. R. Nowak and A. V. Tkachenko, Phys. Rev. E **59**, 3094 (1999).  
[15] P. R. Van Tassel et al, J. Chem. Phys. **112**, 1483 (2000).  
[16] J. Talbot, G. Tarjus and P. Viot, Phys. Rev. E **61** 5429 (2000).  
[17] Lj. Budinski-Petkovic, U. Kozmidis-Lubiric, Physica A **301**, 174 (2001).  
[18] L. Onsager, Ann. N. Y. Acad. Sci., **51**, 627 (1949).  
[19] J. P. Straley, Physical Review A, **4**, 675 (1971).  
[20] D. R. Nelson in *Phase Transitions and Critical Phenomena* edited by C. Domb and J. L. Lebowitz (Academic London, 1983) vol. 7.  
[21] K. Binder in *Monte Carlo Methods in Statistical Physics: An Introduction*, K. Binder, D.W. Heermann (Springer, Berlin, 1988).  
[22] H. Weber, D. Marx and K. Binder, Phys. Rev. B **51**, 14636 (1995).  
[23] S. F. Edwards and D. R. Wilkinson, Proc. Roy. Soc. Lond. A **381**, 17 (1982).  
[24] K. Binder in *Spin Glasses and Random Fields* edited by A. P. Young (World Scientific, 1997).  
[25] Y. -K. Yu, P. L. Taylor and E. M. Terentjev, Phys. Rev. Lett., **81**, 128 (1998).  
[26] We are grateful to Yashodhan Hatwalne, Gautam Menon and Sriram Ramaswamy for very useful inputs on this section.